Observation of Self-Similar Behavior of the 3D, Nonlinear Rayleigh-Taylor Instability

O. Sadot,[1,2,3] V. A. Smalyuk,[1] J. A. Delettrez,[1] D. D. Meyerhofer,[1,4] T. C. Sangster,[1]
R. Betti,[1,4] V. N. Goncharov,[1] and D. Shvarts[2,3]

[1]*Laboratory for Laser Energetics, University of Rochester, 250 East River Road, Rochester, New York 14623, USA*
[2]*NRCN, Beer Sheva 84190, Israel*
[3]*Ben Gurion University of the Negev, Beer Sheva 84015, Isarel*
[4]*Departments of Mechanical Engineering and Physics and Astronomy, University of Rochester, Rochester, New York 14623, USA*
(Received 4 August 2005; published 21 December 2005)

The Rayleigh-Taylor unstable growth of laser-seeded, 3D broadband perturbations was experimentally measured in the laser-accelerated, planar plastic foils. The first experimental observation showing the self-similar behavior of the bubble size and amplitude distributions under ablative conditions is presented. In the nonlinear regime, the modulation σ_{rms} grows as $\alpha_\sigma g t^2$, where g is the foil acceleration, t is the time, and α_σ is constant. The number of bubbles evolves as $N(t) \propto (\varpi t\sqrt{g} + C)^{-4}$ and the average size evolves as $\langle\lambda\rangle(t) \propto \varpi^2 g t^2$, where C is a constant and $\varpi = 0.83 \pm 0.1$ is the measured scaled bubble-merging rate.

DOI: 10.1103/PhysRevLett.95.265001 PACS numbers: 52.35.Py, 52.50.Jm, 52.70.La

The Rayleigh-Taylor (RT) [1,2] instability is a subject of intensive experimental and theoretical research because of its critical importance in inertial confinement fusion (ICF) [3] and astrophysics [4]. In astrophysics, the RT instability is a key component for the understanding of supernova evolution. When a star becomes a supernova, the outer shell is pushed by the inner exploding core and, because of the mixing process, heavy material from the inner shells appears in the outer envelope. In ICF, an imploding outer spherical shell is pushed by an intense radiation field toward the center. The nuclear fuel inside the shell compresses and heats until reaching ignition conditions. The RT instability developed on the fuel-shell surface can lead to target disruption and the degradation of implosion performance [3].

In the linear regime of the instability, small initial modulations grow exponentially in time with growth rates of $\gamma = (Akg)^{0.5}$ for classical RT instability [5–7] and $\gamma = \alpha(kg)^{0.5} - \beta k V_a$ for ablative RT instability [8,9], where k is the modulation wave number, g is the target acceleration, A is the Atwood number, V_a is the ablation velocity, and α and β are constants. Most ICF-related cases involve ablative drive, in which the growth rate is stabilized by the ablation term $\beta k V_a$. The growth rates of the linear RT instability have been calculated and measured in both classical [10] and ablative regimes [10–14]. The first indication of nonlinear RT effects is that the modulations develop into bubbles (penetration of the lighter fluid into the heavier) and spikes (penetration of the heavier fluid into the lighter). There are two modeling approaches for nonlinear RT instability. Modal models predict modulation growth in Fourier space [15,16], while bubble competition models predict modulation growth in the real space [17–24]. Both types of models predict that the average modulation size shifts to longer wavelengths as the modulations grow. In Fourier space, the amplitudes of the shorter-wavelength modulation saturate at lower levels, while longer-wavelength modulations continue to grow and achieve higher velocities before they saturate. As a result, the spectral peak of the modes in Fourier space develops and shifts to longer wavelengths [25], as predicted by Haan's model [15].

Bubble competition models are generally used in more advanced nonlinear stages where the interaction between neighboring bubbles governs the modulation evolution. These models predict that smaller bubbles (with smaller nonlinear velocities) are overcome by larger bubbles (with higher nonlinear velocities) through bubble competition and bubble merger processes [5,20–24]. These models are based on the bubble merger concept and predict that the bubble size reaches self-similar behavior by looking at the growth of the mixing zone. These models also predict that the average size of modulations shifts to longer wavelengths as the modulations grow. Experiments in the turbulent regime of classical RT instability [7], supported by computer simulations [5,21–24], show that average bubble amplitudes grow as $\alpha g t^2$ in the highly nonlinear regime, where the constant α may depend on the initial conditions [24]. Our experiments take advantage of the most quantitative and descriptive method for modulation measurements—face-on, x-ray radiography [25,26]—and measure the nonlinear evolution near saturation in detail before modulations enter a highly nonlinear regime. By measuring the individual size and amplitude of each bubble, the distributions of bubble sizes and amplitudes were constructed, and the self-similarity of these distributions was observed. As a result of this self-similarity, the rich and complex physics of nonlinear RT instability can be described simply and comprehensively in real space through the evolution of bubble sizes and amplitudes in addition to the growth of the mixing region, used in earlier research.

In the experiment, CH targets (with thicknesses ranging from 20 to 90 μm) were driven by 12 ns square laser pulses

at an intensity of $\sim 5 \times 10^{13}$ W/cm^2 on the OMEGA Laser System [27]. Initial 3D, broadband modulations were created by the nonuniformities of the individual laser drive beams [25,26]. As the hot and light plasma (created by laser ablation) accelerates the cold and dense plasma of the central part of the target, the interface between the light and dense plasma (the ablation surface) is unstable and the modulations on this interface grow because of RT instability. Backlighter x rays were used to measure the growing target modulations. The transmitted x rays propagated through the target and were then imaged by a pinhole array onto a framing camera, allowing time-resolved (with $\sim$80 ps temporal resolution) images of the target modulations to be recorded with a spatial resolution of ~ 10 μm. Details of the experimental setup are presented in Refs. [25,26]. Figure 1 shows the central portions of the recorded images of the target modulations. The window size is 333 μm $\times$ 333 μm. Images in Figs. 1(a)–1(c) were recorded at different times with target distances traveled of 1, 18, and 67 μm. The light areas (higher x-ray transmission) represent bubbles, while the dark areas (lower x-ray transmission) represent spikes. As the modulations grow, the average bubble size shifts to longer wavelengths, big bubbles become bigger, and small bubbles disappear, as evident from the images in Fig. 1.

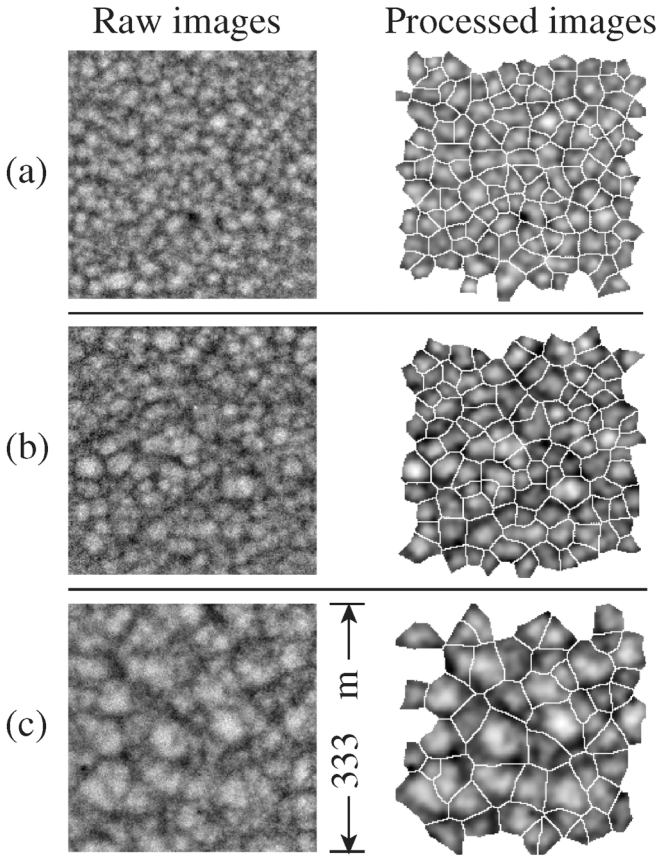

FIG. 1. X-ray radiographs of growing 3D broadband modulations measured with x-ray radiography recorded at target distances traveled of (a) 1, (b) 18, and (c) 67 μm in 20-, 35-, and 55 μm-thick CH foils. The corresponding Wiener-filtered images with imposed bubble borders (found using the watershed algorithm) are shown on the right-hand side. The light areas (more x-ray transmission) represent bubbles, while dark areas (less x-ray transmission) represent spikes.

To measure bubble characteristics such as size and amplitude, the images were processed with the watershed algorithm [28] to determine the bubble edges. Examples of this procedure are shown in the right-hand side of Figs. 1(a)–1(c), where the bubble borders are superimposed on the Weiner-filtered images [26]. The bubbles near the edges of analysis regions were excluded from the analysis because the sizes and amplitudes of these bubbles could not be accurately determined. The bubble size λ was calculated using $\lambda = 2(S/\pi)^{0.5}$, where S is the bubble area. The evolution of the distributions of bubble sizes λ and their rms amplitudes a [corresponding to images in Figs. 1(a)–1(c)] are shown in Figs. 2(a) and 2(b), respectively. As modulations grow, the number of bubbles decreases while their average size and average rms amplitude increase. The measured distributions of bubble sizes and amplitudes were fitted with the normal

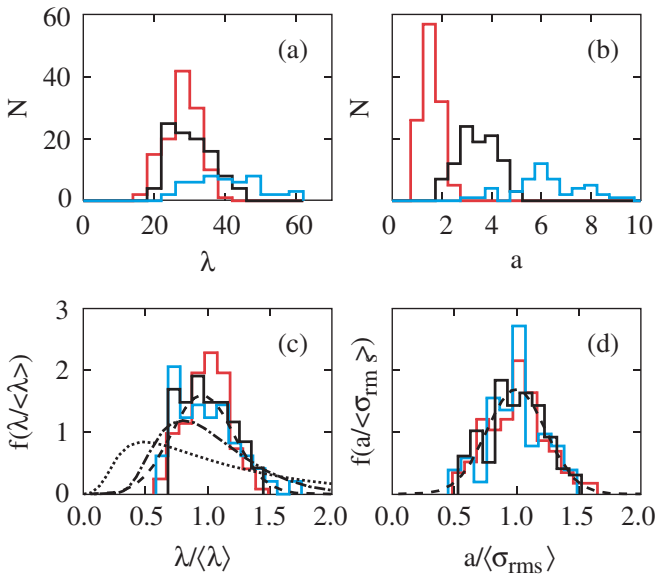

FIG. 2 (color). (a) Distributions of the bubble sizes and (b) the bubble rms amplitudes measured at three different distances traveled—1 μm (red curve), 18 μm (black curve), and 67 μm (blue curve). (c) The normalized bubble size distributions as in (a) presented as a function of normalized bubble size. (d) Normalized bubble rms amplitude distributions as a function of normalized rms amplitude at the same distance traveled. The similarity between the normalized distributions suggests that the instability is in the self-similar regime where the normalized distributions do not change. The dashed curves represent normal distribution fits to the measured data. The dotted and dot-dashed lines in (c) are the distributions predicted from the 2D and 3D models, respectively, presented in Refs. [5,29,30].

distribution from which average size $\langle\lambda\rangle$ and average rms amplitude $\langle\sigma\rangle$ were determined. Figures 2(c) and 2(d) show the normalized distributions [from Figs. 2(a) and 2(b)] as functions of normalized bubble size $\lambda/\langle\lambda\rangle$ and normalized amplitude $a/\langle\sigma\rangle$. The dashed lines in Figs. 2(c) and 2(d) represent fits to the experimental data using normal distributions $f_\sigma(a/\langle\sigma\rangle) = \exp[-(a/\langle\sigma\rangle - 1)^2/2C_a^2]/\sqrt{2\pi}C_a$ for bubble amplitude and $f_\sigma(\lambda/\langle\lambda\rangle) = \exp[-(\lambda/\langle\lambda\rangle - 1)^2/2C_\lambda^2]/\sqrt{2\pi}C_\lambda$ for the bubble size distributions, where $C_\lambda = 0.24 \pm 0.01$ and $C_a = 0.23 \pm 0.01$ are constants determined from these fits. Both bubble size and amplitude distributions are in the self-similar regime because the normalized distributions do not change in time. The self-similarity of RT growth is explicitly measured in our experiments by the evolution of bubble size and amplitude distributions, while in earlier simulations and experiments, the self-similarity was inferred from the growth of the size of the mixing zone. The dotted and dot-dashed lines in Fig. 2(c) are the distributions predicted from the 2D and 3D models, respectively [presented in Refs. [5,29,30]]. As expected, the 3D model prediction is a better representation of the experimental results.

The evolutions of the average size $\langle\lambda\rangle$ and the average rms amplitude $\langle\sigma\rangle$ also compare very well with self-similar growth where these quantities are expected to grow proportionally to gt^2 (g is the target acceleration and t is time). Figure 3 shows the measured evolution of the total number of bubbles N [Fig. 3(a)] and the average bubble size $\langle\lambda\rangle$ [Fig. 3(b)] as a function of the distance traveled by the driven target $d = 1/2gt^2$. The distance traveled represents the amount of the growth because the growth factors are related to the distance traveled. Following Refs. [5,29,30], we assume that the total number of bubbles N decreases with the scaled average merging rate ϖ according to

$$\frac{dN}{dt} = -\sqrt{\frac{g}{\langle\lambda\rangle(t)}}\varpi N(t). \tag{1}$$

The conservation of the total area of all bubbles leads to the following equation for the evolution of the average bubble size $\langle\lambda\rangle$:

$$\frac{d\langle\lambda\rangle}{dt} = \sqrt{\frac{g}{\langle\lambda\rangle}}\frac{\varpi}{2}\langle\lambda\rangle. \tag{2}$$

The solutions to these equations are $N(t) = D(\varpi t\sqrt{g} + 2C)^{-4}$ and $\langle\lambda\rangle(t) = \varpi^2 gt^2/16 + \sqrt{g}t\varpi C/4 + C^2/4$, respectively. In Figs. 3(a) and 3(b) these solutions are plotted as fits to the experimental data (solid lines). The constants D and C are related to the initial average bubble size $\langle\lambda\rangle_0$ and the initial number of bubbles N_0, respectively, as $D = N_0(2C)^4$ and $C = 2\sqrt{\langle\lambda\rangle_0}$. From the fit to the data, it was found that $N_0 = 230 \pm 10$ and $\langle\lambda\rangle_0 = 27 \pm 1$ μm. The same scaled average merging rate $\varpi = 0.83 \pm 0.1$ was found (using the two fits independently) when two generations of bubble change, corresponding to the reduction in the number of bubbles by factor of $\sim$4.

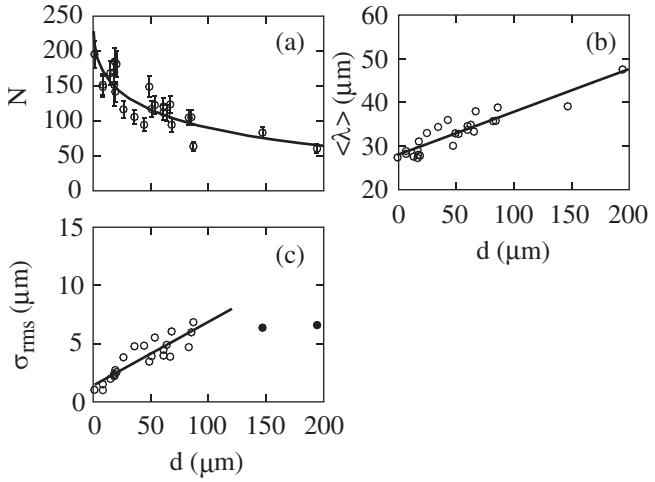

FIG. 3. (a) The measured number of bubbles (circles) as a function of the distance traveled. The solid line is the fit of Eq. (1) to the experimental data. (b) The measured average bubble size (circles) as a function of the distance traveled. The solid line is the linear fit to the data. The normalized merging rates, as determined independently using fit curves in (a) and (b), are the same. (c) The $\sigma_{\rm rms}$ of the modulations (circles) as a function of the distance traveled. The solid line is the linear fit to the data excluding the two filled points in which the density calculated by 1D hydrocode LILAC is affected by 3D effects.

Figure 3(c) shows the evolution of the modulation $\sigma_{\rm rms}$ as a function of the distance traveled. It was calculated by dividing the measured $\sigma_{\rm rms}$ of areal-density (target density multiplied by its thickness) modulations by the calculated [using 1D hydrocode LILAC [31]] target density. The solid line is the linear fit to the data without the two filled points, showing that the modulation $\sigma_{\rm rms}$ growing as $\alpha_\sigma gt^2$, where $\alpha_\sigma = 0.027 \pm 0.003$ is the constant determined from the fit. To find the bubble front growth we assumed [15,16] that $\alpha_b = \sqrt{2}\alpha_\sigma$, which leads to $\alpha_b = 0.040 \pm 0.004$, consistent with theoretical models [15,16] and nonablative experiments [6,23,24]. The two filled points were excluded from the fit because the analysis based on the Haan saturation model [in Fourier space [15]] showed that the density of the 90 μm-thick target at the very end of acceleration (at $\sim$11 ns, when these two points were measured) is smaller by a factor of 2 than that predicted by LILAC.

The nonlinear RT bubble evolution is rich and complex. As the modulations grow, new bubbles are born as a result of the competition and merger processes. Some bubbles grow larger, while others shrink and disappear. Yet because the measured bubble sizes and rms amplitude distributions are in a self-similar regime, their evolutions can be described by a very simple form based on their measured normal distributions, shown above. The number of bubbles $n(t, a, \lambda)$ in the intervals of a to $a + da$ and λ to $\lambda + d\lambda$ at time t can be expressed as

$$n(t; a, \lambda) = \frac{dad\lambda}{2\pi\langle\lambda\rangle\langle a\rangle C_\lambda C_a} \times N(t) e^{-[(\lambda/\langle\lambda\rangle)-1]^2/2C_\lambda^2} e^{-[a/\langle a\rangle-1]^2/2C_a^2}, \quad (3)$$

where $\langle\lambda\rangle$ and $N(t)$ evolve according to the solution to Eqs. (1) and (2), and the modulation rms amplitudes evolve as $\langle a\rangle = \langle a\rangle_0 + \alpha_\sigma g t^2$.

Previous studies in more-turbulent regimes were able to describe the evolution in terms of the growth of the average modulation levels. Kolmogorov's scaling [22–24], which is another way to describe modulations using their power spectra, is also applied to a highly nonlinear, turbulent regime. The Haan model (which is valid in the weakly nonlinear regime near saturation levels) predicts growth of modulation spectra in Fourier space. Using Eq. (3), we are able to explicitly show the details of the modulation growth of the bubble front in real space. This description is valid in the weakly nonlinear regime because the diagnostic technique used for the measurements (face-on radiography) works in this stage of the RT instability (but not in the highly nonlinear turbulent regime).

In summary, the nonlinear Rayleigh-Taylor evolution of 3D broadband modulations was measured in the nonlinear stage using x-ray face-on radiography. By measuring the individual size and amplitude of each bubble, the distributions of bubble sizes and amplitudes were constructed. These distributions evolve self-similarly as the target modulations grow. During this growth, the modulations shift to longer wavelengths as bubbles compete and merge. The number of bubbles N evolves as $N(t) \propto (\varpi t\sqrt{g} + 2C)^{-4}$, and both the average bubble size and average rms amplitude grow proportionally to gt^2, as predicted by the self-similar growth and scaling theory. This result allows a simple phenomenological model to describe the complex physics of nonlinear RT evolution in the weakly nonlinear regime.

This work was supported by the U.S. Department of Energy Office of Inertial Confinement Fusion under Cooperative Agreement No. DE-FC52-92SF19460, the University of Rochester, and the New York State Energy Research and Development Authority.

[1] L. Rayleigh, Proc. Lond. Math Soc. **14**, 170 (1883).
[2] G. Taylor, Proc. R. Soc. Lond., Ser. A **201**, 192 (1950).
[3] J. D. Lindl, Phys. Plasmas **2**, 3933 (1995).
[4] B. A. Remington *et al.*, Phys. Plasmas **4**, 1994 (1997).
[5] U. Alon *et al.*, Phys. Rev. Lett. **72**, 2867 (1994).
[6] G. Dimonte and M. Schneider, Phys. Fluids **12**, 304 (2000).
[7] K. I. Read, Physica (Amsterdam) **12D**, 45 (1984).
[8] H. Takabe *et al.*, Phys. Fluids **28**, 3676 (1985).
[9] R. Betti *et al.*, Phys. Plasmas **3**, 2122 (1996).
[10] K. S. Budil *et al.*, Phys. Rev. Lett. **76**, 4536 (1996).
[11] S. G. Glendinning *et al.*, Phys. Rev. Lett. **78**, 3318 (1997).
[12] C. J. Pawley *et al.*, Phys. Plasmas **6**, 565 (1999).
[13] J. P. Knauer *et al.*, Phys. Plasmas **7**, 338 (2000).
[14] T. Sakaiya *et al.*, Phys. Rev. Lett. **88**, 145003 (2002).
[15] S. W. Haan, Phys. Rev. A **39**, 5812 (1989).
[16] D. Ofer *et al.*, Phys. Plasmas **3**, 3073 (1996).
[17] D. H. Sharp, Physica (Amsterdam) **12D**, 3 (1984).
[18] C. L. Gardner *et al.*, Phys. Fluids **31**, 447 (1988).
[19] Q. Zhang, Phys. Lett. A **151**, 18 (1990).
[20] J. Glimm and X. L. Li, Phys. Fluids **31**, 2077 (1988).
[21] U. Alon *et al.*, Phys. Rev. Lett. **74**, 534 (1995).
[22] D. L. Youngs, Phys. Fluids A **3**, 1312 (1991).
[23] G. Dimonte *et al.*, Phys. Fluids **16**, 1668 (2004).
[24] G. Dimonte, Phys. Rev. E **69**, 056305 (2004).
[25] V. A. Smalyuk *et al.*, Phys. Rev. Lett. **81**, 5342 (1998).
[26] V. A. Smalyuk *et al.*, Phys. Plasmas **6**, 4022 (1999).
[27] T. R. Boehly *et al.*, Opt. Commun. **133**, 495 (1997).
[28] L. Vincent and P. Soille, IEEE Transactions on Pattern Analysis and Machine Intelligence **13**, 583 (1991).
[29] D. Oron *et al.*, Phys. Plasmas **8**, 2883 (2001).
[30] D. Oron, U. Alon, and D. Shvarts, Phys. Plasmas **5**, 1467 (1998).
[31] J. Delettrez *et al.*, Phys. Rev. A **36**, 3926 (1987).